

Analysis and prediction of shock formation in acoustic energy transfer systems

Vamsi C. Meesala¹, Muhammad R. Hajj², and Shima Shahab ^{*3}

¹Department of Biomedical Engineering and Mechanics, Virginia Tech, 495 Old Turner Street, Norris Hall, Blacksburg, VA 24060, USA

²Department of Civil, Environmental and Ocean Engineering, Davidson laboratory, Stevens Institute of Technology, 711 Hudson Street, Hoboken, NJ 07030, USA

³Department of Mechanical Engineering, Virginia Tech, 635 Prices Fork Road, Goodwin Hall, Blacksburg, VA 24060, USA

Abstract

Losses associated with nonlinear wave propagation and exhibited by acoustic wave distortion and shock formation compromise the efficiency of contactless acoustic energy transfer systems. As such, predicting the shock formation distance and its dependence on the amplitude of the excitation is essential for their efficiency, design and operation. We present an analytical approach capable of predicting the shock formation distance of acoustic waves generated by a baffled disk with arbitrary deformation in a weakly viscous fluid medium. The loss-less Westervelt equation, used to model the nonlinear wave propagation, is asymptotically expanded based on the amplitude of the excitation. Because the solutions of the first- and second-order equations decay at different rates, we implement the method of renormalization and introduce a coordinate transformation to identify and eliminate the secular terms. The approach yields two partial differential equations that can be solved to predict the formation distance either analytically or numerically much faster than time-domain numerical simulations. The analysis and results are validated with solutions obtained from a nonlinear finite element simulation and previous experimental measurements.

Keywords: Nonlinear wave propagation, Method of renormalization, Acoustic shock, Acoustic energy transfer, Contactless energy transfer.

1 Introduction

Acoustic energy transfer (AET) is a transformative contactless energy transfer (CET) technology that utilizes acoustic waves to transfer energy between piezoelectric transducers. AET systems have been shown to outperform conventional electromagnetic CET technologies [1–6] in critical applications [7, 8]. In particular, AET has been proposed to recharge and communicate with low-power (e.g., $1\mu\text{W}$ - 10mW) implanted medical devices [9–11], which eliminates the need for surgery to replace batteries [11–17]; to develop battery-free underwater sensing networks to observe ocean conditions, track migration and habitats of marine animals, and monitor oil spills [8, 18–22]. These applications present the need to developing mathematical and numerical models capable of assessing the efficiency of AET systems [23–37]. In general, most of the current approaches neglect nonlinear effects associated with acoustic wave propagation [38] and the electro-elastic response of the piezoelectric transmitters and receivers [39, 40]. On the other hand, these effects become significant as the source strength is increased to enable higher energy transfer. As such, there is a need to expand the analysis capabilities to models that account for nonlinear effects and investigate their impact on the efficiency of energy transfer systems. In our previous

*Address all correspondence to this author. E-mail address: sshahab@vt.edu

work, we investigated theoretically the effect of material nonlinearity of a piezoelectric receiving disk on the energy transfer. We showed that the material nonlinearity can shift the optimum load resistance and that the shift is a function of the source strength [29]. We have also shown experimentally that the interplay of all the nonlinearities and the standing wave effects between the transmitter and receiver in an AET system can manifest themselves in a complex manner and have an impact on the energy transfer efficiency [36].

One consequence of nonlinear acoustic wave propagation is exhibited by the distortion of its waveform due to a difference in the traveling speeds of the compression and rarefaction parts of the wave. In the frequency domain, this distortion is interpreted as energy transfer from the fundamental wave frequency to its higher harmonics. The accumulation of the distortion effect as the wave travels results in a discontinuity, referred to as a shock [38]. The occurrence of a shock is associated with significant loss in energy that is proportional to the cube of the difference in pressure across the discontinuity. This loss compounds as the wave propagates further resulting in further reduction of the acoustic power [41]. It is relevant to point out here that in a weakly viscous fluid such as water and air, shocks occur before the attenuation is significant [42]. In other words, attenuation effects can be neglected, and a lossless second-order wave equation can be used to analyze the nonlinear wave propagation. In the case of a finite amplitude plane wave, the amplitudes of the higher harmonics grow at the expense of the amplitude of the fundamental or excitation frequency up to the initial shock formation location \bar{x} . Beyond \bar{x} , all components decay due to the energy dissipated as a consequence of the shock propagation [42]. In the context of AET, the component of pressure at the excitation frequency p_ω , that is generated by the transmitting disk operating under high excitation voltage decreases as the distance from the disk is increased due to diffraction and transfer of energy to higher harmonics. However, the total acoustic power remains conserved up to \bar{x} . Beyond \bar{x} , in addition to the transfer of energy and diffraction, the decrease in p_ω will be compounded by additional losses in energy due to the formation and propagation of shocks. In AET systems, the power transfer efficiency depends mostly on the pressure associated with the excitation frequency, p_ω , as the higher harmonics do not necessarily coincide with the higher modes of the receiver [37]. As such, the power transfer efficiency will be significantly compromised beyond \bar{x} , which renders this distance as an essential design parameter for high-intensity AET power transfer.

Analytical expressions for \bar{x} are readily available for plane waves, spherical waves, and on the axis of a focused Gaussian beam [42, 43], which is not the case in AET system where the disk undergoes transverse deformations. Several numerical and analytical studies investigated nonlinear wave propagation and shock characteristics of acoustic wave generated by disks [44–51]. The numerical simulations provide an accurate description of the response. However, they are computationally expensive, especially when solved in the time-domain. The objective of this effort is to develop an analytical approach to predict shock formation associated with a propagating acoustic wave generated by a vibrating disk with arbitrary transverse displacement. We consider an axisymmetric-baffled-vibrating piezoelectric disk and use the Westervelt equation to investigate the associated nonlinear wave propagation. In particular, we scale the governing equation and boundary conditions with ϵ and obtain analytical expressions for the ϵ -order and ϵ^2 -order solutions using the Rayleigh integral. Next, we follow the work of Kelly and Nayfeh [52] with some modifications to eliminate the secular terms by implementing the method of renormalization [53, 54] and obtain a uniformly valid solution of the Westervelt equation. We validate the predictions of the analytical approach with higher fidelity finite element simulations and previously published experimental results.

2 Analysis

An axisymmetric baffled piezoelectric disk with thickness h , and radius a , in a semi-infinite fluid medium is considered to analyze the nonlinear wave propagation of its generated acoustic wave as shown schematically in Fig. 1. The schematic defines Cartesian (x, y, z) , cylindrical (r_p, ψ, z) , and spherical coordinate

(r, θ, ψ) systems with the origin at the center of the disk O_c . An additional spherical coordinate system (r_s, θ_s, ψ) with origin, O_s , at $z = r_0$ is also defined and used in the analysis. The disk is actuated using a dynamic potential difference $V(t)$ across its flat surfaces at a frequency near that of its thickness mode. The resulting axisymmetric radial and transverse displacements are represented by $\hat{u}(r_p, z, t)$, and $\hat{w}(r_p, z, t)$ respectively. The transverse displacement of the thickness mode is chosen because it has a non-zero mean and is therefore favorable for generating acoustic pressure field [34, 55].

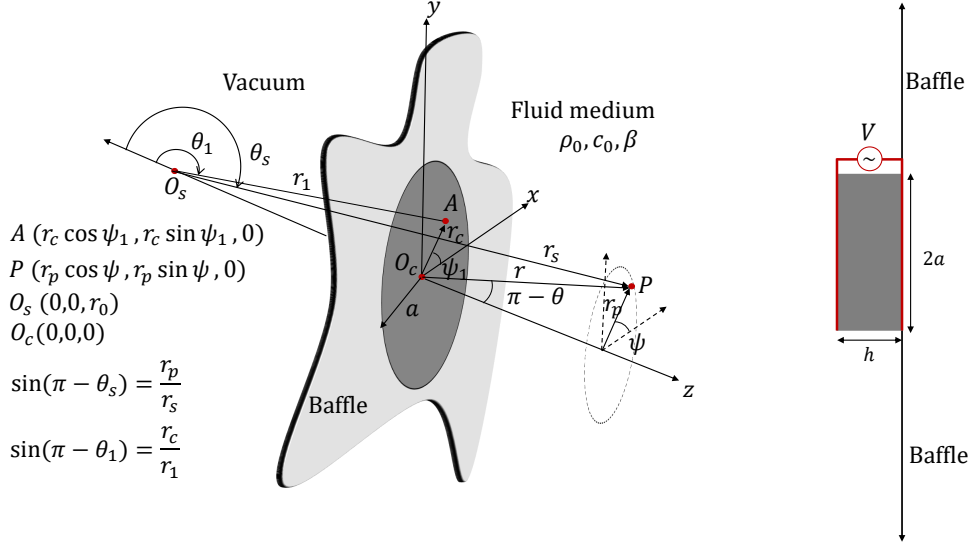


Figure 1: Schematic of the baffled disk with thickness h , and radius a in a semi-infinite fluid medium.

The normal velocity continuity condition at the piezo-medium interface yields the necessary radiation boundary condition written as

$$\frac{\partial}{\partial t}[z - w(r_p, t)] + \nabla\phi(r_p, z, t) \cdot \nabla[z - w(r_p, t)] = 0 \quad (1)$$

where $w(r_p, t) = \hat{w}(r_p, z, t)|_{z=0}$ and $\phi(r_p, z, t)$ is the velocity potential of the fluid. This boundary condition is an approximation because the displacement, written using the Lagrangian description, would have to be mapped to an equivalent Eulerian description to obtain the exact boundary condition. Still, this approximation is acceptable because $r_p \gg \hat{u}(r_p, z, t)|_{z=0}$, except at $r_p = 0$ where $\hat{u}(r_p, z, t)|_{z=0} = 0$, and, consequently, the effects of the approximation are insignificant. Because the modal deformation of the disk can take a complicated shape and does not possess a closed form expression [55], we write $w(r_p, t)$ as

$$w(r_p, t) = \begin{cases} -\epsilon \left(\frac{c_0}{\omega}\right) \cos(\omega t) G(r_p) e^{i\phi(r_p)} & 0 \leq r_p \leq a \\ 0 & r_p > a \end{cases} \quad (2)$$

where ϵ , c_0 , and ω are respectively the acoustic Mach number, velocity of sound in fluid, and excitation frequency, and $G(r_p)$, and $\phi(r_p)$ are respectively the displacement amplitude and phase as a function of the distance r_p .

The loss-less form of the Westervelt equation is used to analyze the nonlinear and non-planar wave propagation of the acoustic pressure $p(r_p, z, t)$. It is written as

$$c_0^2 \nabla^2 p(r_p, z, t) - \frac{\partial^2}{\partial t^2} p(r_p, z, t) = -\frac{\beta}{\rho_0 c_0^4} \frac{\partial^2}{\partial t^2} p(r_p, z, t)^2 \quad (3)$$

where ρ_0 and β are respectively the density and the coefficient of nonlinearity of the fluid. It is relevant to note that the loss-less form is valid if the analysis is restricted to distances smaller than $1/\alpha - \bar{x}_\epsilon$, where α

is the absorption loss parameter of the fluid and \bar{x}_ϵ is the shock formation distance for a plane wave [42]. To solve equation 3 subjected to the boundary condition given by equation 1, we asymptotically expand the pressure as

$$p(r_p, z, t, \epsilon) = \epsilon p_1(r_p, z, t) + \epsilon^2 p_2(r_p, z, t) + O(\epsilon^3) \quad (4)$$

and the velocity potential as

$$\phi(r_p, z, t, \epsilon) = \epsilon \phi_1(r_p, z, t) + \epsilon^2 \phi_2(r_p, z, t) + O(\epsilon^3) \quad (5)$$

Substituting the assumed expansions of $p(r_p, z, t)$ and $\phi(r_p, z, t)$ into equations 1, and 3 yields the ϵ -order equation:

$$\frac{\partial^2}{\partial t^2} p_1(r_p, z, t) - c_0^2 \nabla^2 p_1(r_p, z, t) = 0, \quad (6a)$$

and the corresponding boundary condition:

$$\left. \frac{\partial}{\partial z} \phi_1(r_p, z, t) \right|_{z=0} = c_0 \sin(\omega t) G(r_p) e^{i\phi(r_p)}, \quad (6b)$$

and the ϵ^2 -order equation:

$$\frac{\partial^2}{\partial t^2} p_2(r_p, z, t) - c_0^2 \nabla^2 p_2(r_p, z, t) = \frac{\beta}{\rho_0 c_0^4} \frac{\partial^2}{\partial t^2} p_1(r_p, z, t)^2 \quad (6c)$$

From Rayleigh's or KH integral, the pressure generated due to a baffled-vibrating surface of surface area S_0 and transverse velocity $U_0 e^{i\omega t}$ is given by [56, 57]

$$p = \frac{1}{2} \frac{i \rho_0 \omega}{2\pi} \int_{S_0} \frac{U_0}{R} e^{i[\omega t - kR]} dS_0 + c.c \quad (7)$$

where R is the distance between the observation point and an infinitesimal point on the surface (AP in Fig. 1) and $k = \omega/c_0$. As such, the ϵ -order solution is given by

$$p_1(r_p, z, t) = \frac{\rho_0 \omega c_0}{4\pi} e^{i\omega t} \int_0^{2\pi} \int_0^a \frac{1}{R} e^{i[-kR + \phi(r_p)]} G(r_p) r_p dr_p d\psi_1 + c.c \quad (8)$$

The ϵ -order solution in equation 8 contains the independent variables r_p and z inside the integral. Hence, a partial differential equation with an integral forcing function needs to be solved to determine the ϵ^2 -order solution. Such a solution is not straightforward. To simplify the analysis, we rewrite $p_1(r_p, z, t)$ in terms of an infinite series as suggested by Hasegawa et al. [58], using the spherical coordinate system (r_s, θ_s, ψ) with the origin at $z = r_0$ (see Fig. 1), as

$$p_1(r_s, \theta_s, t) = \frac{\rho_0 \omega c_0}{4\pi} e^{i\omega t} \int_0^{2\pi} \int_0^a \frac{1}{R} e^{i[-kR + \phi(r_p)]} G(r_p) r_p dr_p d\psi_1 + c.c \quad (9a)$$

where

$$R = \sqrt{r_s^2 + r_1^2 - 2r_s r_1 \cos \gamma} \quad (9b)$$

and

$$\cos \gamma = \cos \theta_s \cos \theta_1 + \sin \theta_s \sin \theta_1 \cos(\psi - \psi_1). \quad (9c)$$

Following Hasegawa et al. [58], equation 9a is modified to

$$p_1(r_s, \theta_s, t) = -\frac{i \rho_0 \omega c_0 k}{2} e^{i\omega t} \sum_{n=0}^{\infty} \Delta_n (2n+1) h_n^{(2)}(kr_s) P_n(\cos \theta_s) + c.c \quad (9d)$$

where

$$\Delta_n = \int_{r_0}^{r_a} j_n(kr_1) P_n(\cos \theta_1) G(r_1) e^{j\phi(r_1)} r_1 dr_1, \quad (9e)$$

$r_1^2 = r_p^2 + r_0^2$, and $r_a^2 = a^2 + r_0^2$, P_n is the Legendre function and $h_n^{(2)}$ is the spherical Hankel function of the second kind, which is defined by $h_n^{(2)} = j_n - iy_n$ where j_n and y_n are respectively the spherical Bessel functions of the first and second kind. For subsequent analysis, the ϵ -order solution is converted from exponential to trigonometric form and written as

$$p_1(r_s, \theta_s, t) = \rho_0 k c_0 \omega \sum_{n=0}^{n=\infty} (2n+1) P_n(\cos \theta_s) \left(\Delta_n^{(c)} [\sin(\omega t) j_n(kr_s) - \cos(\omega t) y_n(kr_s)] \right. \\ \left. + \Delta_n^{(s)} [\cos(\omega t) j_n(kr_s) + \sin(\omega t) y_n(kr_s)] \right) \quad (9f)$$

where

$$\Delta_n^{(c)} = \int_{r_0}^{r_a} j_n(kr_1) P_n(\cos \theta_1) G \cos(\phi(r_1)) r_1 dr_1 \quad (9g)$$

$$\Delta_n^{(s)} = \int_{r_0}^{r_a} j_n(kr_1) P_n(\cos \theta_1) G \sin(\phi(r_1)) r_1 dr_1 \quad (9h)$$

Substituting the ϵ -order solution in the ϵ^2 -order equation (6c) yields

$$\frac{\partial^2}{\partial t^2} p_2(r_s, \theta_s, t) - c_0^2 \nabla^2 p_2(r_s, \theta_s, t) = -2 \sum_{n=0}^{\infty} \sum_{m=0}^{\infty} (2n+1)(2m+1) k^4 \beta \rho \omega^2 P_n(\cos \theta_s) P_m(\cos \theta_s) \\ \times \left(E_1 \cos(2\omega t) + E_2 \sin(2\omega t) \right) \quad (10a)$$

where

$$E_1 = \left(\Delta_n^{(c)} \Delta_m^{(c)} - \Delta_n^{(s)} \Delta_m^{(s)} \right) \left(j_n(kr_s) j_m(kr_s) - y_n(kr_s) y_m(kr_s) \right) \\ + \left(\Delta_n^{(c)} \Delta_m^{(s)} + \Delta_n^{(s)} \Delta_m^{(c)} \right) \left(j_m(kr_s) y_n(kr_s) + j_n(kr_s) y_m(kr_s) \right), \text{ and} \quad (10b)$$

$$E_2 = \left(\Delta_n^{(c)} \Delta_m^{(c)} - \Delta_n^{(s)} \Delta_m^{(s)} \right) \left(j_m(kr_s) y_n(kr_s) + j_n(kr_s) y_m(kr_s) \right) \\ - \left(\Delta_n^{(c)} \Delta_m^{(s)} + \Delta_n^{(s)} \Delta_m^{(c)} \right) \left(j_n(kr_s) j_m(kr_s) - y_n(kr_s) y_m(kr_s) \right) \quad (10c)$$

To obtain the analytical expression for the ϵ^2 -order solution, the product of Legendre functions is rewritten as [52]

$$P_n(\cos \theta_s) P_m(\cos \theta_s) = \sum_{q=0}^{p+n} \kappa_{qnm} P_q(\cos \theta_s) \quad (11)$$

where the coefficient κ_{qnm} is determined from the orthogonality condition of the Legendre-functions as

$$\kappa_{qnm} = \frac{2q+1}{2} \int_{-1}^1 P_q(x) P_n(x) P_m(x) dx \quad (12)$$

Substituting equation 11 into equation 10a, we obtain

$$\frac{\partial^2}{\partial t^2} p_2(r_s, \theta_s, t) - c_0^2 \nabla^2 p_2(r_s, \theta_s, t) = -2 \sum_{n=0}^{\infty} \sum_{m=0}^{\infty} \sum_{q=0}^{n+m} (2n+1)(2m+1) k^4 \beta \rho \omega^2 \kappa_{qnm} P_q(\cos \theta_s) \times \left(E_1 \cos(2\omega t) + E_2 \sin(2\omega t) \right) \quad (13)$$

As detailed in Appendix A, the solution of ϵ^2 -order equation (13), $p_2(r_s, \theta_s, t)$, is obtained using the separation of variables. The final solution of the pressure is then written as

$$p(r_s, \theta_s, t, \epsilon) = \epsilon \rho_0 k c_0 \omega \sum_{n=0}^{n=\infty} \Delta_n^{(c)} (2n+1) P_n(\cos \theta_s) [\sin(\omega t) j_n(kr_s) - \cos(\omega t) y_n(kr_s)] + \epsilon \rho_0 k c_0 \omega \sum_{n=0}^{n=\infty} \Delta_n^{(s)} (2n+1) P_n(\cos \theta_s) [\cos(\omega t) j_n(kr_s) + \sin(\omega t) y_n(kr_s)] + \epsilon^2 p_2(r_s, \theta_s, t) + O(\epsilon^3) \quad (14)$$

The ϵ -order and ϵ^2 -order terms in equation 14 decay at different rates with respect to r_s . If left untreated, the ϵ^2 -order terms can become significant and contradict the scaling condition that ϵ -order terms $\gg \epsilon^2$ -order terms. To solve this contradiction and eliminate terms leading to this contradiction, we implement the method of renormalization and introduce the coordinate transformation [52]

$$r_s = \eta + \epsilon f(\eta, \theta_s, t) \quad (15)$$

Substituting the above transformation into equation 14 and applying the Taylor expansion yields

$$p(r_s, \theta_s, t, \epsilon) = \epsilon p_1(\eta, \theta_s, t) + \epsilon^2 f(\eta, \theta_s, t) \left. \frac{\partial}{\partial r_s} p_1(r_s, \theta_s, t) \right|_{r_s=\eta} + \epsilon^2 p_2(\eta, \theta_s, t) + O(\epsilon^3) \quad (16)$$

From equation 16, the necessary condition to eliminate the secular terms is

$$f(\eta, \theta_s, t) \left. \frac{\partial}{\partial r_s} p_1(r_s, \theta_s, t) \right|_{r_s=\eta} + p_2(\eta, \theta_s, t) = 0 \quad (17)$$

The transformation f becomes singular unless there is a particular relation between the phases of p_2 and $\partial p_1 / \partial r_s |_{r_s=\eta}$. To examine the phase relation, we represent p_2 and $\partial p_1 / \partial r_s |_{r_s=\eta}$ respectively as $p_2(\eta, \theta_s, t) = \bar{p}_2(\eta, \theta_s) \cos(2\omega t - 2k\eta + \phi_{p_2})$ and $\partial p_1 / \partial r_s |_{r_s=\eta} = \bar{p}'_1(\eta, \theta_s) \cos(\omega t - k\eta + \phi_{p'_1})$ where $\bar{p}_2(\eta, \theta_s)$, $\phi_{p_2}(\eta, \theta_s)$, $\bar{p}'_1(\eta, \theta_s)$, and $\phi_{p'_1}(\eta, \theta_s)$ are respectively the amplitude and phase of p_2 and amplitude and phase of $\partial p_1 / \partial r_s |_{r_s=\eta}$. From equation 17, $f(\eta, \theta_s, t)$ is then determined as

$$f(\eta, \theta_s, t) = \frac{2\bar{p}_2(\eta, \theta_s)}{\bar{p}'_1(\eta, \theta_s)} \cos(\pi/4 - \omega t + k\eta - \phi_{p_2}(\eta, \theta_s)/2) \left[\cos(-\pi/4 + \phi_{p'_1} - \phi_{p_2}(\eta, \theta_s)/2) + \tan(\pi/2 - \omega t + k\eta - \phi_{p'_1}) \sin(-\pi/4 + \phi_{p'_1}(\eta, \theta_s) - \phi_{p_2}(\eta, \theta_s)/2) \right] \quad (18)$$

It is evident from equation 18 that singularities arise in f because of the tangent functions, unless $\phi_{p'_1} - \phi_{p_2}/2 = \pi/4$. However, $\phi_{p'_1}$ and ϕ_{p_2} do not always hold such a relation. To eliminate this singularity, we rewrite $p_2(\eta, \theta_s, t)$ as

$$p_2(\eta, \theta_s, t) = 2 \frac{\bar{p}_2(\eta, \theta_s)}{\bar{p}'_1(\eta, \theta_s)} \left. \frac{\partial p_1}{\partial r} \right|_{r=\eta} \cos\left(\omega t - k\eta + \phi_{p_2}(\eta, \theta_s) - \phi_{p'_1}(\eta, \theta_s)\right) - \bar{p}_2(\eta, \theta_s) \cos\left(\phi_{p_2}(\eta, \theta_s) - 2\phi_{p'_1}(\eta, \theta_s)\right) \quad (19)$$

Then, eliminating the first part on the right hand side of equation 19 and using the remaining time-independent term as a feedback error to the ϵ -order solution yields

$$p(r_s, \theta_s, t, \epsilon) = \epsilon p_1(\eta, \theta_s, t) - \epsilon^2 \bar{p}_2(\eta, \theta_s) \cos(\phi_{p_2}(\eta, \theta_s) - 2\phi_{p'_1}(\eta, \theta_s)) \quad (20)$$

where

$$r_s = \eta + \epsilon f(\eta, \theta_s, t) \quad (21)$$

$$f(\eta, \theta_s, t) = -2 \frac{\bar{p}_2(\eta, \theta_s)}{\bar{p}'_1(\eta, \theta_s)} \cos(\omega t - k\eta + \phi_{p_2}(\eta, \theta_s) - \phi_{p'_1}(\eta, \theta_s)) \quad (22)$$

From equation 22, it is noted that the transformation f is independent of ϵ . This is a powerful consequence of the method of renormalization as once f is determined from p_1 and p_2 , which are again independent of ϵ , it can be used for any value of ϵ .

Equations 20 - 22 constitute the solution of the nonlinear wave propagation of the acoustic pressure generated by a vibrating disk with transverse excitation according to equation 2. For a given r_s , θ_s , and t , one needs to first evaluate f from equation 22 and then solve for η using equation 21. The value of η can then be used to determine the nonlinear pressure from equation 20. As the wave propagates in the medium, equation 21 will eventually yield multiple solutions for η due to the cumulative nature of the nonlinearity [38, 49]. The first location where multiple solutions occur or when the $\partial p / \partial r_s = \infty$ is the shock location [38, 52, 59–61]. Beyond this location, the solution is not valid and a shock fitting criteria such as equal-area rule should be used [38, 53].

3 Validation

The efficacy of the analysis presented in the previous section to predict the nonlinear wave propagation and shock formation is assessed by comparing its predictions with those from (a) higher fidelity Finite Element (FE) simulations and (b) previously published experimental results.

3.1 Comparison with Finite Element simulations

A piezoelectric disk with radius $a = 5$ mm and thickness $h = 2$ mm made of PZT-5H material and submerged in water was considered for validation using numerical simulations. The material and acoustic properties of the disk and fluid are presented in Table 1. The corresponding Rayleigh far-field distance is defined by $r_{far} = 1/2ka^2 = 53.3$ mm. We performed a series of axisymmetric frequency and time-domain FE simulations in COMSOL Multiphysics to obtain the acoustic radiation characteristics of the baffled-disk configuration. A quarter-circular fluid domain of radius r_f was considered in the simulations. A spherical wave radiation boundary condition at the outer boundary was used to simulate an infinitely propagating wave.

Table 1: Material properties of the disk and fluid. C^E , e , and ε^S are respectively the the stiffness at constant electric field, coupling parameter, and relative permittivity at constant strain matrices.

Parameter [units]	Value
Density of the disk, ρ [kg/m ³]	7500
C_{11}^E [GPa]	127.21
C_{12}^E [GPa]	80.21
C_{13}^E [GPa]	84.67
C_{33}^E [GPa]	117.44
C_{44}^E [GPa]	22.99
e_{31} [C/m ²]	-6.63
e_{33} [C/m ²]	23.24
e_{24} [C/m ²]	17.03
ε_{11}^S	1704.4
ε_{33}^S	1433.6
Density of the fluid, ρ_0 [kg/m ³]	999.6
Velocity of sound in the fluid, c_0 [m/s]	1481.44
Nonlinear parameter of the fluid, β	3.6

3.1.1 Linear acoustic radiation

In both analysis and simulations, the material and geometric nonlinearities of the disk are neglected. Furthermore, because of the presence of a baffle, only the transverse displacement of the top surface of the disk is required to determine its acoustic radiation. In the simulations, we extracted this displacement from a linear FE simulation and use it as a boundary condition in the nonlinear FE simulation for computational efficiency, realized by eliminating the multiphysics coupling between the piezoelectric and fluid domains.

Considering a maximum mesh size of $\lambda_{f_0}/6$ in the fluid domain and 20 elements each along the radius and thickness of the disk, we solved the linear problem using frequency domain FE solver and determined that the thickness mode resonant frequency of the disk is $f_0 = 1.005$ MHz, where $\lambda_{f_0} = c_0/f_0$. The response and radiation characteristics of the disk for an excitation voltage amplitude corresponding to $\epsilon = 10^{-5}$ and an excitation frequency of f_0 are presented in Fig. 2. In particular, Figs. 2a-2d show respectively the sound pressure level ($p_{ref} = 1$ Pa) in the fluid domain, deformation of the disk, transverse displacement of the top surface of the disk, and beam pattern at different radial distances from the origin (see schematic in Fig. 2a). The abnormal higher deformation amplitude on the bottom surface compared to the top surface of the disk in Fig. 2b is due to the absence of radiation damping, unlike the top surface. From Fig. 2d, we note that except for $r = 0.125r_{far}$, the pressure along the z -axis is maximum for any r value. Consequently, we expect the shock to occur first on the z -axis. We also note that $r = 0.125r_{far}$ is a local minimum, similar to those observed in the near-field of axial pressure generated by a piston [46, 57, 62]. Because we expect the shock to occur along the z -axis first, we limit further analysis only to the axial pressure distribution.

3.1.2 Nonlinear axial acoustic wave propagation

Next, the transverse displacement presented in Fig. 2c is used to obtain axial p_1 and p_2 according to the solution in section 2. Alternatively, p_1 and p_2 could be determined by solving the ϵ -order and ϵ^2 -order

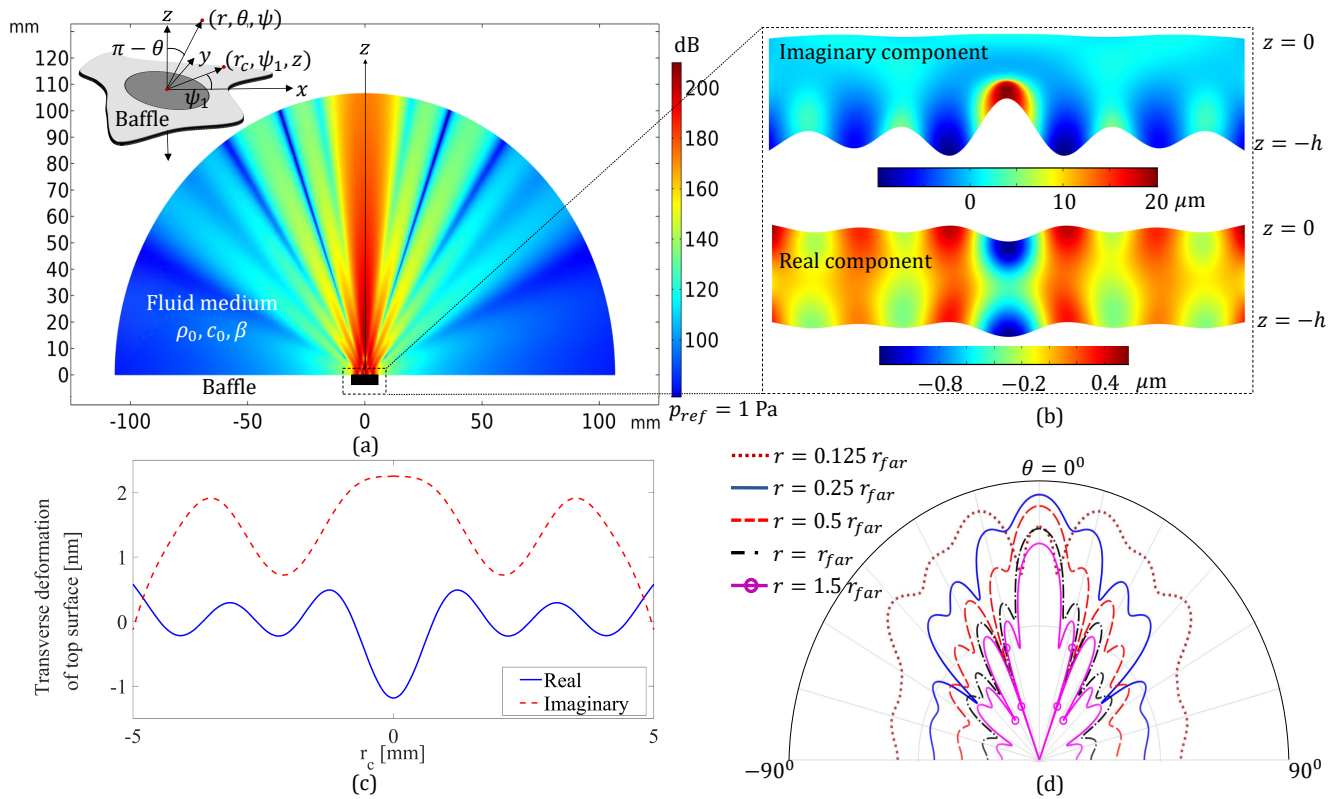


Figure 2: (a) The sound pressure level ($p_{ref} = 1 \text{ Pa}$) in the fluid domain, (b) real and imaginary components of the deformation of the disk, (c) transverse displacement of the top surface of the disk, and (d) beam (directivity) pattern at different radial distances from the origin, for $\epsilon = 10^{-5}$ at an excitation frequency of 1.005 MHz.

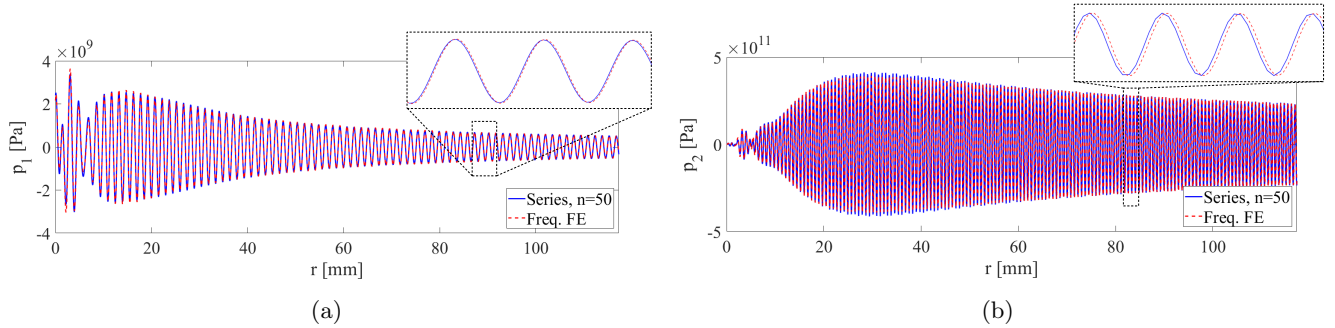
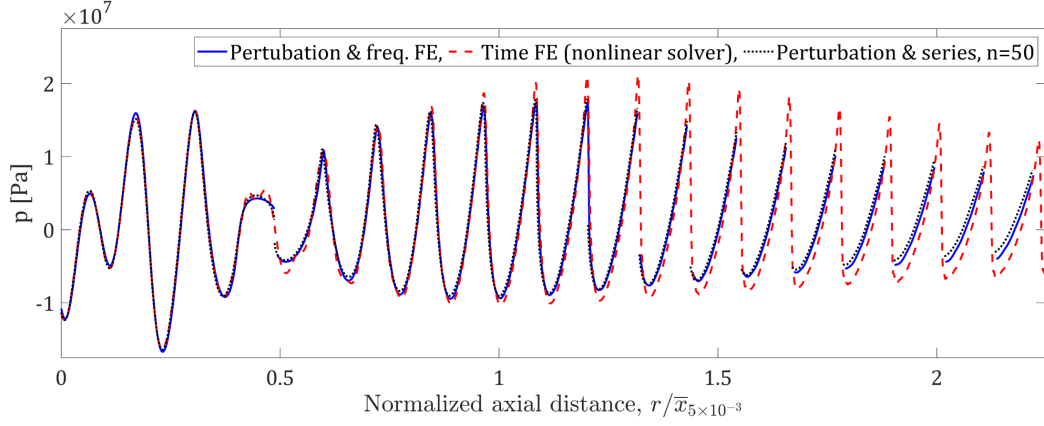


Figure 3: Comparison of axial (a) ϵ -order solution p_1 , and (b) ϵ^2 -order solution p_2 , determined by using the analysis developed for $n = 50, r_0 = -50/k$ and by a frequency domain FE solver. The analytical solution is labeled as Series, $n = 50$ and FE solution is labeled as Freq. FE. On z -axis, $r_s = r - r_0$ and $\theta = \theta_s = \pi$.

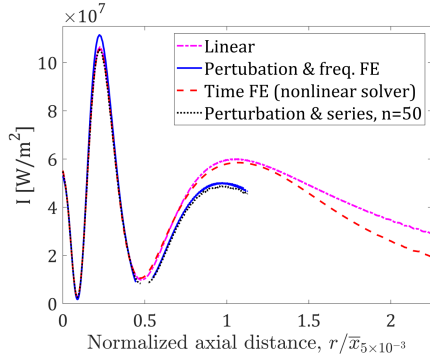
equations and ϵ -order boundary condition in a frequency domain FE solver. A pressure release boundary condition on the disk should be used to solve the ϵ^2 -order equations to ensure that p_2 vanishes on the surface of the disk. We note that p_2 evaluated using the two approaches should differ only by the non-secular terms (NST) that were neglected in the analysis. The axial p_1 and p_2 evaluated from the model for $n = 50, r_0 = -50/k$, labeled as Series $n = 50$, and by the frequency domain FE simulations are presented respectively in Fig. 3(a) and Fig. 3(b). A mesh size of $\lambda_{f_0}/12$ was used in the FE simulations. Fig. 3(a) shows an excellent agreement between p_1 evaluated by the analysis and numerical simulations except at close distances to the disk. The disagreement in this region is due to limiting the series and can be minimized by choosing higher values of n and r_0 . From Fig. 3(b), we note a close agreement in the amplitude and a small phase shift. We attribute this shift to errors induced by choosing a finite value of n , and to the contribution of the NST. It is relevant to point out that p_1 and p_2 determined using FE are more accurate and that eliminating p_2 that includes NST in the method of the renormalization will result in a transformation that will account for the complete particular solution of the ϵ^2 -order equation. As for computational cost, the evaluation of p_1 and p_2 from the analysis requires the analytical expressions of integrals presented in Appendix A and storing, reusing, and manipulation of these expressions, which can become computationally expensive, especially for higher values of n . On the other hand, the linear frequency domain FE simulations to determine p_1 and p_2 is more efficient as it involves a matrix inversion. Moreover, the FE solver can be easily extended to complicated geometries.

Having determined p_1 and p_2 , we compare next the nonlinear wave propagation predicted using equations 20 - 22 with that determined from a nonlinear time-domain FE simulation for three different excitation levels, namely $\epsilon = 5 \times 10^{-3}$, $\epsilon = 2.5 \times 10^{-3}$, and $\epsilon = 1.25 \times 10^{-3}$. Towards that objective, we constructed a fluid domain of $r_f = 2.25 \times \bar{x}_\epsilon$ that is excited by the transverse displacement presented in Fig. 2c. A maximum mesh size of $\lambda_{f_0}/36$ was selected so that the response at $6f_0$ can be captured. For the sake of completeness, Westervelt equation with dissipation was simulated in time-domain using COMSOL Multiphysics by choosing the diffusivity of the sound as $\delta = 1.34 \times 10^{-6} \text{ m}^2/\text{s}$. However, the absorption is not expected to have a significant impact on the response because the characteristic absorption distance ($1/\alpha = 2c_0^3/(\delta\omega^2)$) for f_0 is about 120 m, which is significantly larger than $2.25 \times \bar{x}_{1.25 \times 10^{-3}} (\approx 0.1 \text{ m})$.

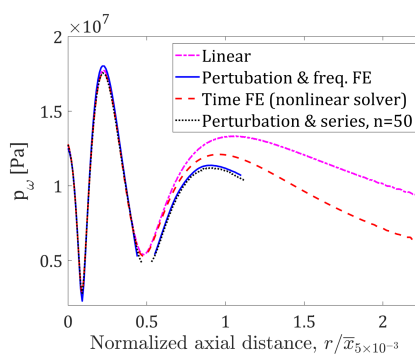
The steady-state response characteristics for $\epsilon = 5 \times 10^{-3}$ obtained using time-domain FE simulation and from equations 19 - 22 using p_1 and p_2 as determined from the analysis (Perturbation & series, $n = 50$) and frequency domain FE simulations (Perturbation & freq. FE) are compared next. The plots presented in Figs. 4(a) - 4(d) show respectively the steady-state axial pressure waveform at time $t = 1/(2f_0)$, the mean intensity, amplitude of the pressure component with frequency $\omega = 2\pi f_0$, and the amplitude of the pressure component with frequency 2ω . Figs. 4(b) and 4(c) also show respectively the mean intensity and pressure when $\beta = 0$, i.e., for the linear case. Based on the closeness of the



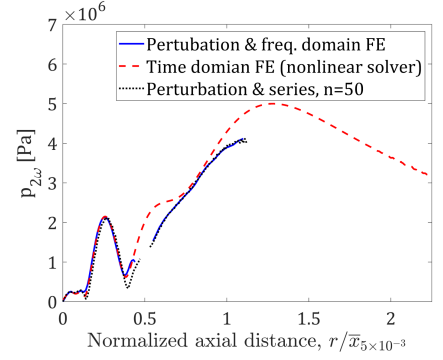
(a)



(b)



(c)



(d)

Figure 4: Comparison of steady-state axial (a) pressure waveform at time $t = 1/(2f_0)$, (b) mean intensity, (c) component of the pressure at $\omega = 2\pi f_0$, and (d) component of the pressure at 2ω obtained from time-domain FE simulation and from the model developed when p_1 and p_2 are obtained from the analysis (Perturbation & series, $n = 50$) and from frequency domain simulations (Perturbation & freq. FE) for $\epsilon = 5 \times 10^{-3}$ and an excitation frequency $f_0 = 1.005$ MHz. The axial distance is normalized with the corresponding characteristic shock formation distance $\bar{x}_5 \times 10^{-3} = 13.03$ mm.

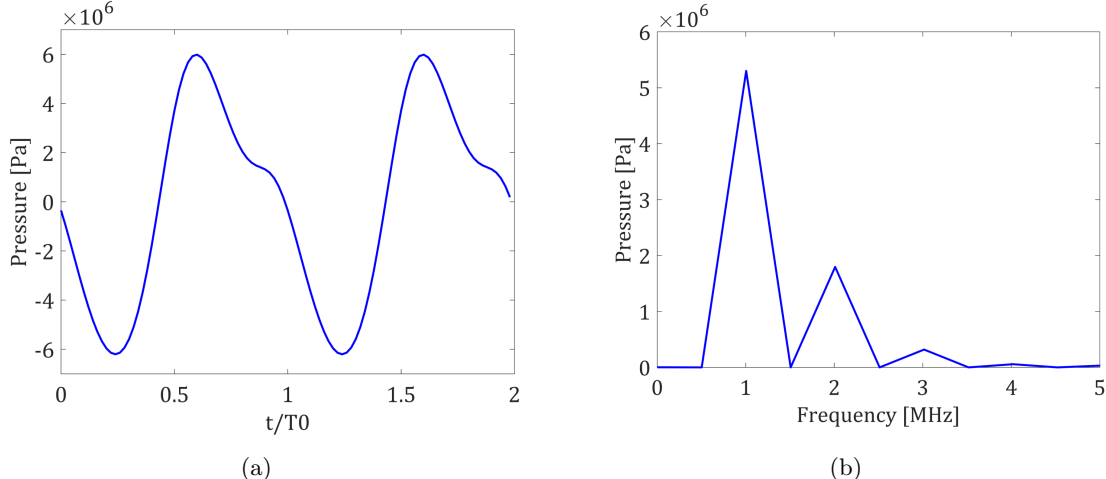
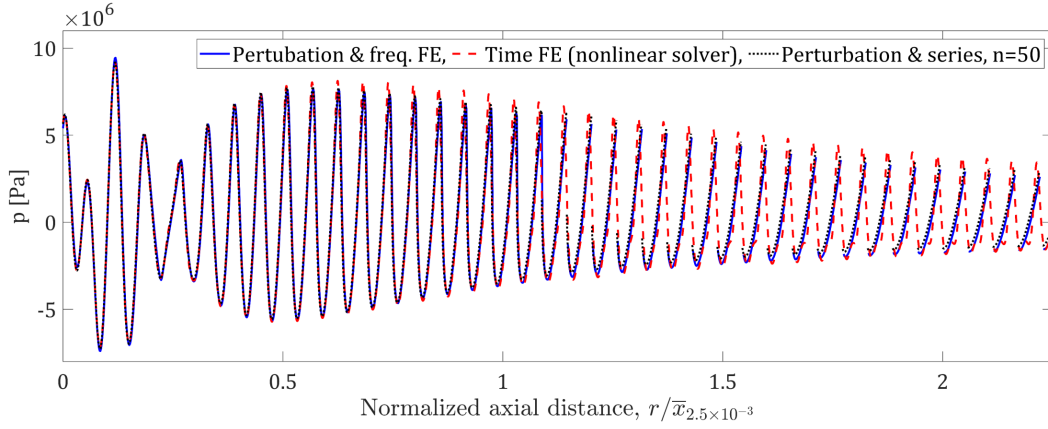


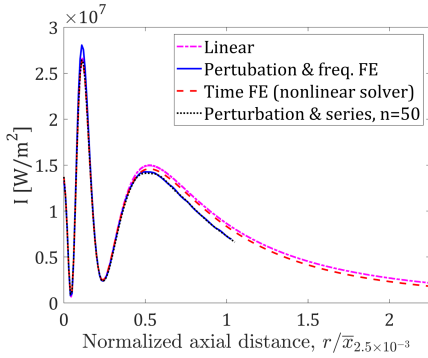
Figure 5: The (a) time series and (b) amplitude Fourier coefficients of the pressure at $r/\bar{x}_{5 \times 10^{-3}} = 0.48$ on z -axis for $\epsilon = 5 \times 10^{-3}$ and excitation frequency $f_0 = 1.005$ MHz obtained from a time-domain FE simulation. Here, $\bar{x}_{5 \times 10^{-3}} = 13.03$ mm.

responses predicted when p_1 and p_2 are determined from the analysis and from the FE simulations, it can be concluded that the contribution of NST is not significant. It can also be concluded that the transformation does an excellent job in predicting the pressure distributions at closer distances and that the discrepancies grow as the distance increases. The discrepancy is because the ϵ^3 -order secular terms become dominant as the distance increases to the point where one needs to carry the method of renormalization to ϵ^3 -order to maintain the accuracy. Figs. 4(a) - 4(d) also show regions where the transformation yields multiple solutions, which invalidates the solution and as such no solution is shown. As noted in previous studies [38, 53], these regions correspond to the shock formation and a shock fitting criteria should be used to obtain the true waveform in these regions. From the results, the transformation yields multiple solutions in a small region around $r/\bar{x}_{5 \times 10^{-3}} = 0.5$, and when $r/\bar{x}_{5 \times 10^{-3}} > 1.13$. However, from Fig. 4(b), the mean intensity predicted by the time-domain FE simulation deviates from the linear case only beyond $r/\bar{x}_{5 \times 10^{-3}} = 1.13$. This deviation is a consequence of loss of energy due to the formation and propagation of shock [38, 46]. As such, we hypothesize that $r/\bar{x}_{5 \times 10^{-3}} = 1.13$ is the shock formation location for $\epsilon = 5 \times 10^{-3}$. As expected, an accelerated decrease in p_{ω} is seen after the shock formation at $r/\bar{x}_{5 \times 10^{-3}} = 1.13$ in Fig. 4(c). To confirm that a shock didn't occur around $r/\bar{x}_{5 \times 10^{-3}} = 0.5$, we present the time series and Fourier coefficients of the pressure at $r/\bar{x}_{5 \times 10^{-3}} = 0.48$ as obtained from the time-domain FE simulation respectively in Figs. 5(a) and 5(b). The Fourier component of pressure at $2f_0$ is comparable with that at f_0 in Fig. 5(b), the corresponding time series presented in Fig. 5(a) doesn't indicate a shock, confirming that no shock occurs in the region around $r/\bar{x}_{5 \times 10^{-3}} = 0.5$. We attribute this anomaly predicted by the model to the local minima in the amplitude of pressure, which is essentially a singularity. As such, multiple solutions are also associated with local minima of the pressure amplitude in the near field. To the knowledge of the authors, this conclusion has not been made in previous investigations as the pressure fields analyzed in those studies did not exhibit local minima.

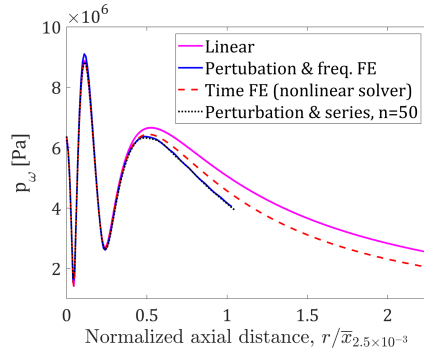
The steady-state axial pressure waveform at time $t = 0$, mean intensity, component of pressure at ω , and the component of pressure at 2ω akin to Figs. 4(a) - 4(d) for the case of $\epsilon = 2.5 \times 10^{-3}$ are respectively presented in Figs. 6(a) - 6(d). The agreement of the results obtained from the analysis and time-domain FE simulation is similar to that observed in Figs. 4(a) - 4(d). The only major difference is the absence of an anomaly, which suggests that the occurrence of anomaly also depends on the magnitude of ϵ . More importantly, the results predicted by the analysis suggest that the shock formation location on the z -axis is $r/\bar{x}_{2.5 \times 10^{-3}} = 1.04$, which is also the point after which the mean intensity predicted by the time-domain FE simulation deviates from the linear case. The characteristic shock formation distance for



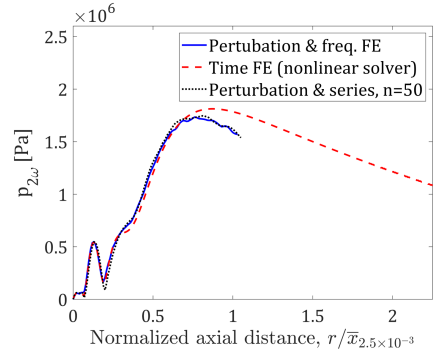
(a)



(b)



(c)



(d)

Figure 6: Comparison of steady-state axial (a) pressure waveform at time $t = 0$, (b) mean intensity, (c) component of the pressure at $\omega = 2\pi f_0$, and (d) component of the pressure at 2ω obtained from time-domain FE simulation and from the model developed when p_1 and p_2 are obtained from the analysis (Perturbation & series, $n = 50$) and from frequency domain simulations (Perturbation & freq. FE) for $\epsilon = 2.5 \times 10^{-3}$ and excitation frequency $f_0 = 1.005$ MHz. The axial distance is normalized with the corresponding characteristic shock formation distance $\bar{x}_{2.5 \times 10^{-3}} = 26.07$ mm.

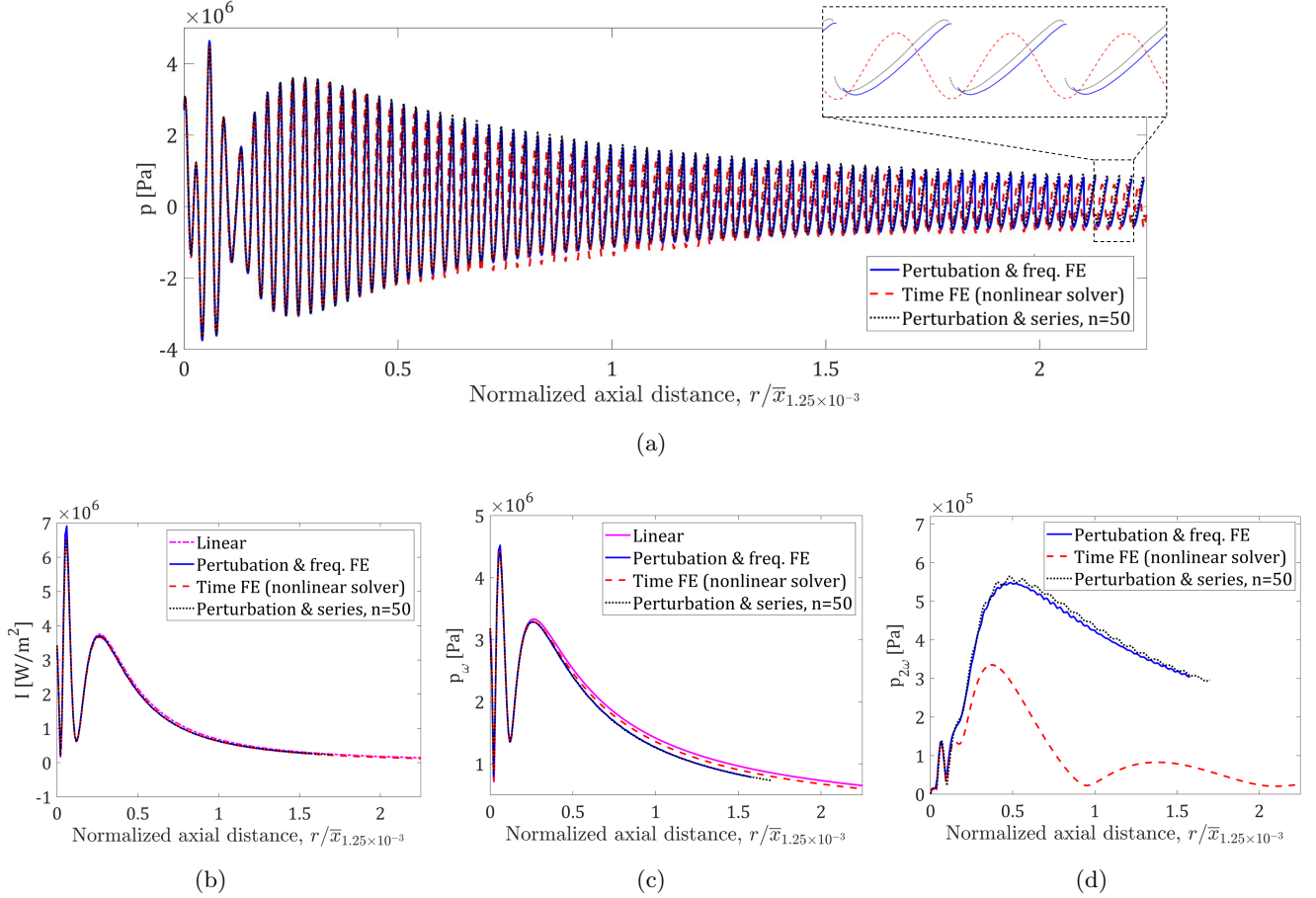


Figure 7: Comparison of steady-state axial (a) pressure waveform at time $t = 0$, (b) mean intensity, (c) component of the pressure at $\omega = 2\pi f_0$, and (d) component of the pressure at 2ω obtained from time-domain FE simulation and from the model developed when p_1 and p_2 are obtained from analysis (Perturbation & series, $n = 50$) and from frequency domain simulations (Perturbation & freq. FE) for $\epsilon = 1.25 \times 10^{-3}$ and excitation frequency $f_0 = 1.005$ MHz. The axial distance is normalized with the corresponding characteristic shock formation distance $\bar{x}_{1.25 \times 10^{-3}} = 52.13$ mm.

$\epsilon = 2.5 \times 10^{-3}$ is $\bar{x}_{2.5 \times 10^{-3}} = 26.07$ mm.

The results for the case of excitation amplitude $\epsilon = 1.25 \times 10^{-3}$ are presented in Figs. 7(a) - 7(d). Inspecting the steady-state axial pressure waveform at time $t = 0$ predicted by time-domain FE simulation in Fig. 7(a), we note that a shock does not take place in the range of $0 < r < 2.25 \times \bar{x}_{1.25 \times 10^{-3}}$, where $\bar{x}_{1.25 \times 10^{-3}} = 52.13$ mm. This result can also be inferred from Fig. 7(b), which doesn't show any deviation of the mean intensity predicted by the time-domain FE simulation from the linear case. Consequently, the deviation of p_ω obtained from time-domain FE simulation from the linear case in Fig. 7(c) is very small. The results predicted by the analysis suggest that the shock formation location on the z -axis is around $r/\bar{x}_{1.25 \times 10^{-3}} = 1.64$, which falls in the far-field region of the disk. This inconsistency is again a consequence of implementing the method of renormalization only up to the $O(\epsilon^2)$ order, as discussed earlier.

3.2 Comparison with previous experiments

The efficacy of the developed model in predicting the nonlinear wave propagation and shock formation location is also validated by comparing its predictions with the experimental data of Nachef et al. [62].

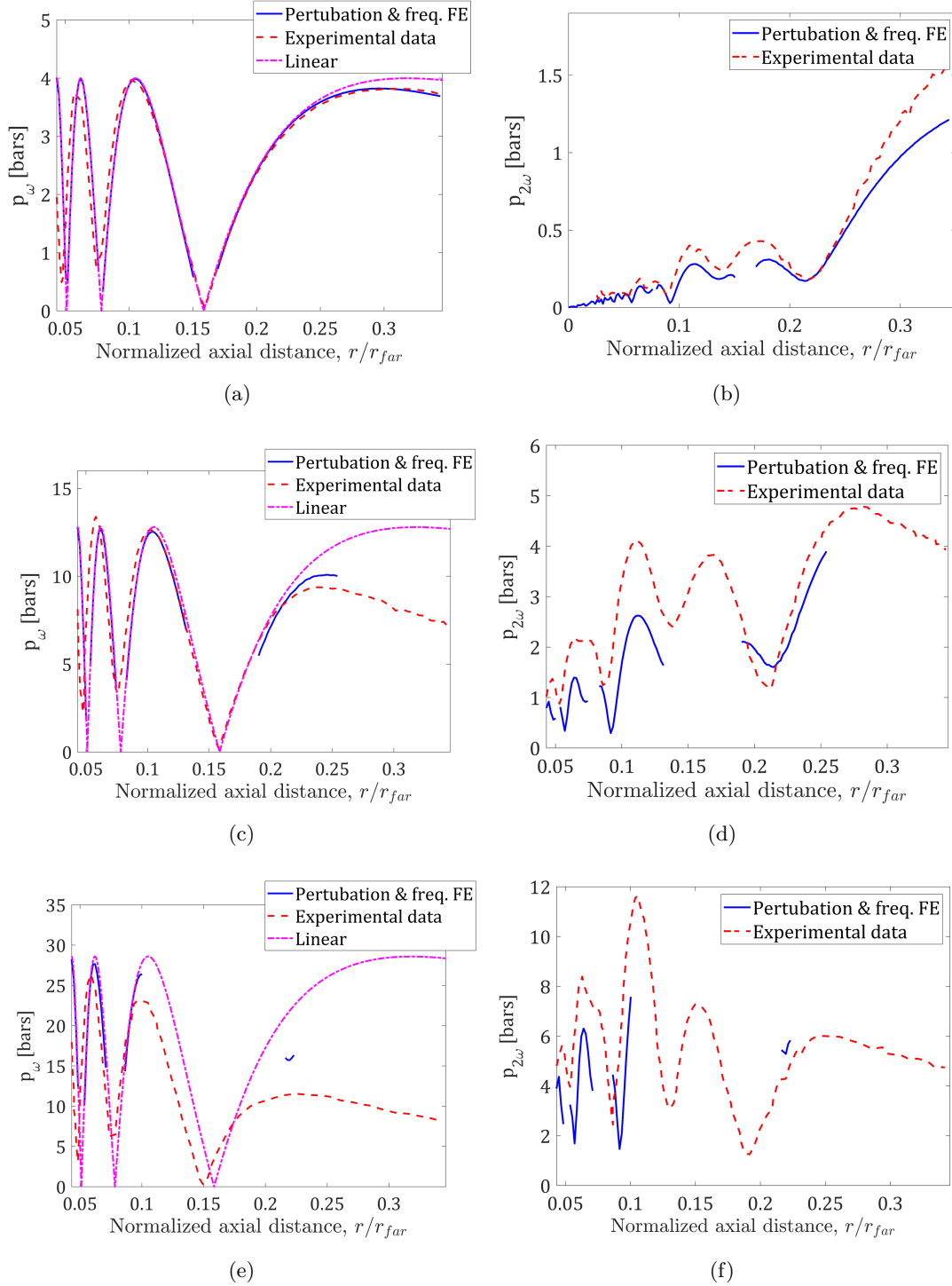


Figure 8: Comparisons of Fourier components of the axial pressure generated by a baffled piston at ω and 2ω predicted using equations 20 - 22 (Perturbation & freq. FE) with the linear case ($\beta = 0$) and corresponding experimental data respectively when (a,b) $p_0 = 0.2$ MPa, (c,d) $p_0 = 0.64$ MPa, and (e,f) $p_0 = 1.43$ MPa. The axial distance is normalized using the Rayleigh far-field distance $r_{\text{far}} = 1156.63$ mm and the experimental data is extracted from Khokhlova et al. [46]

Nachef et al. considered a piezoelectric ceramic disk having a radius of 25 mm and measured the pressure waveforms over axial distances between 50 mm and 400 mm, and lateral distances of between 0 mm and 50 mm for different source strengths at an excitation frequency of $f_0 = 1$ MHz. These waveforms were later treated as a benchmark by Khokhlova et al. [46] to validate their numerical models for $p_0 = 0.2, 0.64,$ and 1.43 MPa where $p_0 = \epsilon\rho_0c_0^2$ is the amplitude of the pressure at the source. They identified that the shock formation distances on the axis are respectively $0.1r_{far}$ and $0.28r_{far}$ for $p_0 = 1.43$ MPa and $p_0 = 0.64$ MPa where the Rayleigh far-field distance $r_{far} = 1156.63$ mm. They concluded that a shock didn't occur on the axis before 400 mm [46] when $p_0 = 0.2$ MPa. The relevant material and geometric properties were identified as $\rho_0 = 1000$ kg/m³, $c_0 = 1500$ m/s, $\beta = 3.5$, and the equivalent aperture of the circular piston as $a = 23.5$ mm [46].

From the discussion in Section 3.1.2, p_1 and p_2 can be evaluated either by the analysis or from appropriate frequency domain linear FE simulations. For the sake of simplicity, we evaluated p_1 and p_2 using the FE simulations to determine the nonlinear wave propagation generated by a baffled piston. Figs. 8(a) - 8(b) show respectively the comparisons of Fourier components of pressure at ω and 2ω predicted using equations 20 - 22 with the linear case ($\beta = 0$) and corresponding experimental data when $p_0 = 0.2$ MPa. The corresponding results for $p_0 = 0.64$ MPa and $p_0 = 1.43$ MPa are presented respectively in Figs. 8(c) - 8(d) and Figs. 8(e) - 8(f). From the results, we note the shock formation distances predicted by the method of renormalization are $r/r_{far} = 0.25$, and $r/r_{far} = 0.1$ respectively for $p_0 = 0.64$ MPa and $p_0 = 1.43$ MPa and that a shock did not occur in the range considered for $p_0 = 0.2$ MPa. These findings are very close to the shock formation distances identified by Khokhlova et al. [46], which validate the analysis.

4 Conclusions

The knowledge of the shock formation distance is very crucial for AET systems and the analysis developed in this work provides a quick estimate that can aid the design and operation of efficient AET systems. The analysis is based on asymptotic expansion of the governing equation. The method of renormalization is used to predict the nonlinear wave generated by a finite amplitude baffled circular disk for a specified deformation profile. The lossless form of the Westervelt equation and the normal velocity continuity boundary condition were scaled with a non-dimensional parameter related to the amplitude of the transverse displacement of the disk. They were expanded and solved by introducing a coordinate transformation to eliminate the secular terms, which resulted in singularities that required redefining the relation between the pressure components. We validated the analysis by comparing its predictions of the shock formation distance under different excitation levels with higher fidelity nonlinear finite element simulations and previously published experimental results. We also demonstrated the versatility of the analysis by showing that the ϵ -order and ϵ^2 -order solutions can be determined either from analytical expressions or from linear frequency domain finite element simulations. We showed that the analysis accurately predicts the nonlinear wave propagation and shock formation distance in the near-field of the disk and argued that the accuracy level can be increased by extending the analysis to ϵ^3 or higher orders. We found out that the transformation yields multiple solutions at the shock location and at local minima that occur in the near-field of the pressure. We also showed an accelerated decrease in the power of the excitation frequency beyond the shock formation. Of particular importance is the validity of the solution for any excitation level because the ϵ and ϵ^2 order solutions are independent of that level.

5 Compliance with Ethical Standards - Conflict of interest

The authors declare that they have no conflict of interest.

6 Acknowledgments

This work was supported by the National Science Foundation Grant No. ECCS–1711139, which is gratefully acknowledged. The authors would also like to thank Professor Saad Ragab (Virginia Tech) for providing valuable feedback in developing the model.

A ϵ^2 –order solution

To determine the particular solution of equation 13, we use the separation of variables technique and assume the solution as

$$p_2(r_s, \theta_s, t) = 2 \sum_{n=0}^{\infty} \sum_{m=0}^{\infty} \sum_{q=0}^{n+m} (2n+1)(2m+1)k^4 \beta \rho \omega^2 \kappa_{qnm} P_q(\cos \theta_s) \left[\sin(2\omega t) \Psi_{qnm}(r_s) + \cos(2\omega t) X_{qnm}(r_s) \right] \quad (23)$$

Substitution of equation 23 in equation 13 yields

$$c_0^2 \left[\frac{1}{r^2} q(q+1) \Psi_{qnm}(r_s) - \frac{2}{r} \frac{\partial \Psi_{qnm}(r_s)}{\partial r_s} - \frac{\partial^2 \Psi_{qnm}(r_s)}{\partial r_s^2} \right] - 4\omega^2 \Psi_{qnm}(r_s) = -E_{\Psi}(r_s) \quad (24a)$$

$$c_0^2 \left[\frac{1}{r^2} q(q+1) X_{qnm}(r_s) - \frac{2}{r} \frac{\partial X_{qnm}(r_s)}{\partial r_s} - \frac{\partial^2 X_{qnm}(r_s)}{\partial r_s^2} \right] - 4\omega^2 X_{qnm}(r_s) = -E_X(r_s) \quad (24b)$$

where

$$E_{\Psi}(r_s) = \left(\Delta_n^{(c)} \Delta_m^{(c)} - \Delta_n^{(s)} \Delta_m^{(s)} \right) \left(j_m(kr_s) y_n(kr_s) + j_n(kr_s) y_m(kr_s) \right) - \left(\Delta_n^{(c)} \Delta_m^{(s)} + \Delta_n^{(s)} \Delta_m^{(c)} \right) \left(j_n(kr_s) j_m(kr_s) - y_n(kr_s) y_m(kr_s) \right) \quad (24c)$$

$$E_X(r_s) = \left(\Delta_n^{(c)} \Delta_m^{(c)} - \Delta_n^{(s)} \Delta_m^{(s)} \right) \left(j_n(kr_s) j_m(kr_s) - y_n(kr_s) y_m(kr_s) \right) + \left(\Delta_n^{(c)} \Delta_m^{(s)} + \Delta_n^{(s)} \Delta_m^{(c)} \right) \left(j_m(kr_s) y_n(kr_s) + j_n(kr_s) y_m(kr_s) \right) \quad (24d)$$

The homogeneous solutions of equations 24a and 24b are $X_1(r_s) = \Psi_1(r_s) = j_q(2kr_s)$ and $X_2(r_s) = \Psi_2(r_s) = y_q(2kr_s)$, which are now used to determine its particular solution by using the variation of parameters technique as

$$\Psi_{qnm}(r_s) = \Psi_1(r_s) \int_{r_0/\cos \theta_s}^{r_s} \frac{\Psi_2(x)}{\Psi_1(x) \frac{\partial \Psi_2(x)}{\partial x} - \Psi_2(x) \frac{\partial \Psi_1(x)}{\partial x}} E_{\Psi}(x) dx - \Psi_2(r_s) \int_{r_0/\cos \theta_s}^{r_s} \frac{\Psi_1(x)}{\Psi_1(x) \frac{\partial \Psi_2(x)}{\partial x} - \Psi_2(x) \frac{\partial \Psi_1(x)}{\partial x}} E_{\Psi}(x) dx \quad (25a)$$

$$X_{qnm}(r_s) = X_1(r_s) \int_{r_0/\cos \theta_s}^{r_s} \frac{X_2(x)}{X_1(x) \frac{\partial X_2(x)}{\partial x} - X_2(x) \frac{\partial X_1(x)}{\partial x}} E_X(x) dx - X_2(r_s) \int_{r_0/\cos \theta_s}^{r_s} \frac{X_1(x)}{X_1(x) \frac{\partial X_2(x)}{\partial x} - X_2(x) \frac{\partial X_1(x)}{\partial x}} E_X(x) dx \quad (25b)$$

where x is a dummy variable. Since the closed form expression of spherical Bessel functions in terms of trigonometric functions are required to identify the secular terms in ϵ^2 -order solution (i.e., $\Psi_{qnm}(r_s)$ and $X_{qnm}(r_s)$), we use an identity of Rayleigh's formula and represent spherical Bessel function of the first kind as

$$j_n(x) = \sum_{n_1=0}^n \begin{bmatrix} n \\ n_1 \end{bmatrix} 2^{n-n_1} \sum_{n_2=0}^{n_1} n_2! \begin{Bmatrix} n_1 \\ n_2 \end{Bmatrix} \sum_{n_3=0}^{n_2} \frac{(-1)^{n+n_2-n_3} x^{-n-1-n_3} \sin(x + n_3\pi/2)}{n_3!} \quad (26)$$

where $\begin{bmatrix} n \\ n_1 \end{bmatrix}$ and $\begin{Bmatrix} n_1 \\ n_2 \end{Bmatrix}$ are respectively the Stirling numbers of the first and second kind. From equation 26, the coefficients of the trigonometric functions can be determined which can then be used to determine $y_n(x)$. By using the so obtained analytical expressions of the spherical Bessel functions, it can be showed that

$$\left[\Psi_1(x) \frac{\partial \Psi_2(x)}{\partial x} - \Psi_2(x) \frac{\partial \Psi_1(x)}{\partial x} \right] = \left[X_1(x) \frac{\partial X_2(x)}{\partial x} - X_2(x) \frac{\partial X_1(x)}{\partial x} \right] = \frac{1}{2kx^2} \quad (27)$$

Using the above relation, equations 25a and 25b are rewritten as

$$\Psi_{qnm}(r_s) = \Psi_1(r_s) \int_{r_0/\cos\theta_s}^{r_s} 2kx^2 \Psi_2(x) E_\Psi(x) dx - \Psi_2(r_s) \int_{r_0/\cos\theta_s}^{r_s} 2kx^2 \Psi_1(x) E_\Psi(x) dx \quad (28a)$$

$$X_{qnm}(r_s) = X_1(r_s) \int_{r_0/\cos\theta_s}^{r_s} 2kx^2 X_2(x) E_X(x) dx - X_2(r_s) \int_{r_0/\cos\theta_s}^{r_s} 2kx^2 X_1(x) E_X(x) dx \quad (28b)$$

Evaluation of integrals in equations 28a and 28b shows that $\Psi_{qnm}(r_s)$ and $X_{qnm}(r_s)$ contain sine-integral, cosine-integral, $1/r_s^{[\dots]}$, and logarithmic terms. Furthermore, it can also be shown that logarithmic terms grow indefinitely for large r_s with respect to ϵ -order solution and are the secular terms. Although the rest of the terms do not grow indefinitely for large r , some of them have a major contribution to the ϵ^2 -order response, especially at closer distances to the disk, and hence govern the nonlinear interaction. As such, we note that an asymptotic form (such as Kelly and Nayfeh [52]) of these expressions will not convey accurate physics. Furthermore, we noticed that sine-integral and cosine-integral terms decay monotonically at a faster rate than logarithmic and $1/r_s^{[\dots]}$ terms and hence we regard them as non-secular terms (NST) and are neglected in the further analysis.

It is relevant to point out that the homogeneous solution of ϵ^2 -order equation that is responsible for satisfying the ϵ^2 -order boundary condition is not considered in the analysis as it represents a freely propagating wave arising from excitation at the boundary and hence doesn't exhibit an unbounded growth (i.e., NST). Moreover, due to equations 25a and 25b, the ϵ^2 -order vanishes on the surface of the disk ($r_s = r_0/\cos\theta_s$). This condition ensures that any transformation defined in the method of renormalization vanishes on the surface of the disk, as is required to describe accurate underlying physics [52]. Furthermore, from the definitions of $\Delta_n^{(c)}$ and $\Delta_n^{(c)}$, we note that they are the only parameters that vary for a different deformation profile and that they are constants of integration in determining $\Psi_{qnm}(r_s)$ and $X_{qnm}(r_s)$. As such, the analytical expressions for these integrals can be utilized to determine p_2 for any deformation pattern.

References

- [1] Villa, J. L., Sallán, J., Llombart, A., and Sanz, J. F. Design of a high frequency inductively coupled power transfer system for electric vehicle battery charge. *Applied Energy* 86, 3 (2009), 355–363.

- [2] Bi, Z., Kan, T., Mi, C. C., Zhang, Y., Zhao, Z., and Keoleian, G. A. A review of wireless power transfer for electric vehicles: Prospects to enhance sustainable mobility. *Applied Energy* 179 (2016), 413–425.
- [3] Maharjan, P., Salauddin, M., Cho, H., and Park, J. Y. An indoor power line based magnetic field energy harvester for self-powered wireless sensors in smart home applications. *Applied energy* 232 (2018), 398–408.
- [4] Jafari, M., Malekjamshidi, Z., and Zhu, J. Design and development of a multi-winding high-frequency magnetic link for grid integration of residential renewable energy systems. *Applied energy* 242 (2019), 1209–1225.
- [5] Yu, X., Sandhu, S., Beiker, S., Sassoon, R., and Fan, S. Wireless energy transfer with the presence of metallic planes. *Applied Physics Letters* 99, 21 (2011), 214102.
- [6] Kim, S., Ho, J. S., Chen, L. Y., and Poon, A. S. Wireless power transfer to a cardiac implant. *Applied Physics Letters* 101, 7 (2012), 073701.
- [7] Roes, M. G., Duarte, J. L., Hendrix, M. A., and Lomonova, E. A. Acoustic energy transfer: A review. *IEEE Transactions on Industrial Electronics* 60, 1 (2013), 242–248.
- [8] Jang, J., and Adib, F. Underwater backscatter networking. In *Proceedings of the ACM Special Interest Group on Data Communication*. 2019, pp. 187–199.
- [9] Valdastrì, P., Susilo, E., Forster, T., Strohhofer, C., Menciassi, A., and Dario, P. Wireless implantable electronic platform for chronic fluorescent-based biosensors. *IEEE transactions on Biomedical Engineering* 58, 6 (2011), 1846–1854.
- [10] Vaiarello, Y., Tatinian, W., Leduc, Y., Veau, N., and Jacquemod, G. Ultra-low-power radio microphone for cochlear implant application. *IEEE Journal on Emerging and Selected Topics in Circuits and Systems* 1, 4 (2011), 622–630.
- [11] Maleki, T., Cao, N., Song, S. H., Kao, C., Ko, S.-C., and Ziaie, B. An ultrasonically powered implantable micro-oxygen generator (imog). *IEEE transactions on Biomedical Engineering* 58, 11 (2011), 3104–3111.
- [12] Lee, K. L., Lau, C.-P., Tse, H.-F., Echt, D. S., Heaven, D., Smith, W., and Hood, M. First human demonstration of cardiac stimulation with transcutaneous ultrasound energy delivery: implications for wireless pacing with implantable devices. *Journal of the American College of Cardiology* 50, 9 (2007), 877–883.
- [13] Charthad, J., Weber, M. J., Chang, T. C., and Arbabian, A. A mm-sized implantable medical device (imd) with ultrasonic power transfer and a hybrid bi-directional data link. *IEEE Journal of solid-state circuits* 50, 8 (2015), 1741–1753.
- [14] Seo, D., Carmena, J. M., Rabaey, J. M., Maharbiz, M. M., and Alon, E. Model validation of untethered, ultrasonic neural dust motes for cortical recording. *Journal of neuroscience methods* 244 (2015), 114–122.
- [15] Charthad, J., Chang, T. C., Liu, Z., Sawaby, A., Weber, M. J., Baker, S., Gore, F., Felt, S. A., and Arbabian, A. A mm-sized wireless implantable device for electrical stimulation of peripheral nerves. *IEEE transactions on biomedical circuits and systems* 12, 2 (2018), 257–270.

- [16] Jiang, L., Yang, Y., Chen, R., Lu, G., Li, R., Xing, J., Shung, K. K., Humayun, M. S., Zhu, J., Chen, Y., et al. Ultrasound-induced wireless energy harvesting for potential retinal electrical stimulation application. *Advanced Functional Materials* (2019), 1902522.
- [17] Baltsavias, S., Van Treuren, W., Weber, M. J., Charthad, J., Baker, S., Sonnenburg, J. L., and Arbabian, A. In vivo wireless sensors for gut microbiome redox monitoring. *arXiv preprint arXiv:1902.07386* (2019).
- [18] Leonard, N. E., Paley, D. A., Davis, R. E., Fratantoni, D. M., Lekien, F., and Zhang, F. Coordinated control of an underwater glider fleet in an adaptive ocean sampling field experiment in monterey bay. *Journal of Field Robotics* 27, 6 (2010), 718–740.
- [19] Domingo, M. C. An overview of the internet of underwater things. *Journal of Network and Computer Applications* 35, 6 (2012), 1879–1890.
- [20] Xu, G., Shen, W., and Wang, X. Applications of wireless sensor networks in marine environment monitoring: A survey. *Sensors* 14, 9 (2014), 16932–16954.
- [21] Akyildiz, I. F., Wang, P., and Lin, S.-C. Softwater: Software-defined networking for next-generation underwater communication systems. *Ad Hoc Networks* 46 (2016), 1–11.
- [22] Li, Z., Desai, S., Sudev, V. D., Wang, P., Han, J., and Sun, Z. Underwater cooperative mimo communications using hybrid acoustic and magnetic induction technique. *Computer Networks* (2020), 107191.
- [23] Ozeri, S., Shmilovitz, D., Singer, S., and Wang, C.-C. Ultrasonic transcutaneous energy transfer using a continuous wave 650 khz gaussian shaded transmitter. *Ultrasonics* 50, 7 (2010), 666–674.
- [24] Shahab, S., and Erturk, A. Contactless ultrasonic energy transfer for wireless systems: acoustic-piezoelectric structure interaction modeling and performance enhancement. *Smart Materials and Structures* 23, 12 (2014), 125032.
- [25] Shahab, S., Gray, M., and Erturk, A. Ultrasonic power transfer from a spherical acoustic wave source to a free-free piezoelectric receiver: Modeling and experiment. *Journal of Applied Physics* 117, 10 (2015), 104903.
- [26] Gorostiaga, M., Wapler, M., and Wallrabe, U. Analytic model for ultrasound energy receivers and their optimal electric loads. *Smart Materials and Structures* 26, 8 (2017), 085003.
- [27] Gorostiaga, M., Wapler, M., and Wallrabe, U. Analytic model for ultrasound energy receivers and their optimal electric loads ii: Experimental validation. *Smart Materials and Structures* 26, 10 (2017), 105021.
- [28] Bakhtiari-Nejad, M., Elnahhas, A., Hajj, M. R., and Shahab, S. Acoustic holograms in contactless ultrasonic power transfer systems: Modeling and experiment. *Journal of Applied Physics* 124, 24 (2018), 244901.
- [29] Meesala, V. C., Hajj, M. R., and Shahab, S. Modeling and identification of electro-elastic nonlinearities in ultrasonic power transfer systems. *Nonlinear Dynamics* (2019), 1–20.
- [30] Basaeri, H., Yu, Y., Young, D., and Roundy, S. A mems-scale ultrasonic power receiver for biomedical implants. *IEEE Sensors Letters* 3, 4 (2019), 1–4.

- [31] Herrera, B., Pop, F., Cassella, C., and Rinaldi, M. Aln pmut-based ultrasonic power transfer links for implantable electronics. In *2019 20th International Conference on Solid-State Sensors, Actuators and Microsystems & Eurosensors XXXIII (TRANSDUCERS & EUROSENSORS XXXIII)* (2019), IEEE, pp. 861–864.
- [32] Basaeri, H., Yu, Y., Young, D., and Roundy, S. Acoustic power transfer for biomedical implants using piezoelectric receivers: effects of misalignment and misorientation. *Journal of Micromechanics and Microengineering* 29, 8 (2019), 084004.
- [33] Allam, A., Sabra, K., and Erturk, A. Aspect ratio-dependent dynamics of piezoelectric transducers in wireless acoustic power transfer. *IEEE Transactions on Ultrasonics, Ferroelectrics, and Frequency Control* (2019).
- [34] Meesala, V. C., Ragab, S., Hajj, M. R., and Shahab, S. Acoustic-electroelastic interactions in ultrasound energy transfer systems: Reduced-order modeling and experiment. *Journal of Sound and Vibration* (2020), 115255.
- [35] Bakhtiari-Nejad, M., Hajj, M. R., and Shahab, S. Dynamics of acoustic impedance matching layers in contactless ultrasonic power transfer systems. *Smart Materials and Structures* 29, 3 (2020), 035037.
- [36] Bhargava, A., Meesala, V. C., Hajj, M. R., and Shahab, S. Nonlinear effects in high-intensity focused ultrasound power transfer systems. *arXiv preprint arXiv:2006.12691* (2020).
- [37] Bhargava, A., and Shahab, S. Contactless acoustic power transfer using high-intensity focused ultrasound. *arXiv preprint arXiv:2006.08054* (2020).
- [38] Hamilton, M. F., Blackstock, D. T., et al. *Nonlinear acoustics*, vol. 237. Academic press San Diego, 1998.
- [39] Leadenham, S., and Erturk, A. Unified nonlinear electroelastic dynamics of a bimorph piezoelectric cantilever for energy harvesting, sensing, and actuation. *Nonlinear Dynamics* 79, 3 (2015), 1727–1743.
- [40] Meesala, V. C., and Hajj, M. R. Identification of nonlinear piezoelectric coefficients. *Journal of Applied Physics* 124, 6 (2018), 065112.
- [41] Rudnick, I. On the attenuation of a repeated sawtooth shock wave. *The Journal of the Acoustical Society of America* 25, 5 (1953), 1012–1013.
- [42] Muir, T., and Carstensen, E. Prediction of nonlinear acoustic effects at biomedical frequencies and intensities. *Ultrasound in medicine & biology* 6, 4 (1980), 345–357.
- [43] Dalecki, D., Carstensen, E. L., Parker, K. J., and Bacon, D. R. Absorption of finite amplitude focused ultrasound. *The Journal of the Acoustical Society of America* 89, 5 (1991), 2435–2447.
- [44] Aanonsen, S. I., Barkve, T., Tjo/tta, J. N., and Tjo/tta, S. Distortion and harmonic generation in the nearfield of a finite amplitude sound beam. *The Journal of the Acoustical Society of America* 75, 3 (1984), 749–768.
- [45] Lee, Y.-S., and Hamilton, M. F. Time-domain modeling of pulsed finite-amplitude sound beams. *The Journal of the Acoustical Society of America* 97, 2 (1995), 906–917.
- [46] Khokhlova, V., Souchon, R., Tavakkoli, J., Sapozhnikov, O., and Cathignol, D. Numerical modeling of finite-amplitude sound beams: Shock formation in the near field of a cw plane piston source. *The Journal of the Acoustical Society of America* 110, 1 (2001), 95–108.

- [47] Ginsberg, J. H. Nonlinear king integral for arbitrary axisymmetric sound beams at finite amplitudes. i. asymptotic evaluation of the velocity potential. *The Journal of the Acoustical Society of America* 76, 4 (1984), 1201–1207.
- [48] Ginsberg, J. H. Nonlinear king integral for arbitrary axisymmetric sound beams at finite amplitude. ii. derivation of uniformly accurate expressions. *The Journal of the Acoustical Society of America* 76, 4 (1984), 1208–1214.
- [49] Coulouvrat, F. Y. An analytical approximation of strong nonlinear effects in bounded sound beams. *The Journal of the Acoustical Society of America* 90, 3 (1991), 1592–1600.
- [50] Froysa, K.-E., and Coulouvrat, F. A renormalization method for nonlinear pulsed sound beams. *The Journal of the Acoustical Society of America* 99, 6 (1996), 3319–3328.
- [51] Foda, M. Axial nonlinear field of a vibrating circular transducer. *Archives of Acoustics* 22, 1 (2014), 59–76.
- [52] Kelly, S. G., and Nayfeh, A. Non-linear propagation of directional spherical waves. *Journal of Sound and Vibration* 72, 1 (1980), 25–37.
- [53] Nayfeh, A. H., and Mook, D. T. *Nonlinear oscillations*. John Wiley & Sons, 2008.
- [54] Nayfeh, A. H. *Perturbation methods*. John Wiley & Sons, 2008.
- [55] Guo, N., Cawley, P., and Hitchings, D. The finite element analysis of the vibration characteristics of piezoelectric discs. *Journal of sound and vibration* 159, 1 (1992), 115–138.
- [56] Kim, Y.-H. *Sound propagation: an impedance based approach*. John Wiley & Sons, 2010.
- [57] Kinsler, L. E., Frey, A. R., Coppens, A. B., and Sanders, J. V. Fundamentals of acoustics. *Fundamentals of Acoustics, 4th Edition, by Lawrence E. Kinsler, Austin R. Frey, Alan B. Coppens, James V. Sanders, pp. 560. ISBN 0-471-84789-5. Wiley-VCH, December 1999.* (1999), 560.
- [58] Hasegawa, T., Inoue, N., and Matsuzawa, K. A new rigorous expansion for the velocity potential of a circular piston source. *The Journal of the Acoustical Society of America* 74, 3 (1983), 1044–1047.
- [59] Nayfeh, A., and Kelly, S. G. Non-linear interactions of acoustic fields with plates under harmonic excitations. *Journal of Sound and Vibration* 60, 3 (1978), 371–377.
- [60] Ginsberg, J. H. Propagation of nonlinear acoustic waves induced by a vibrating cylinder. i. the two-dimensional case. *The Journal of the Acoustical Society of America* 64, 6 (1978), 1671–1678.
- [61] Ginsberg, J. H. Propagation of nonlinear acoustic waves induced by a vibrating cylinder. ii. the three-dimensional case. *The Journal of the Acoustical Society of America* 64, 6 (1978), 1679–1687.
- [62] Nachev, S., Cathignol, D., Tjøtta, J. N., Berg, A. M., and Tjøtta, S. Investigation of a high intensity sound beam from a plane transducer. Experimental and theoretical results. *The Journal of the Acoustical Society of America* 98, 4 (1995), 2303–2323.